3D mesoscale modeling and fracture property study of rubberized self- compacting concrete based on uniaxial tension test

Document Version
Accepted author manuscript

[Link to publication record in Manchester Research Explorer](#)

1 **3D mesoscale modeling and fracture property study of rubberized**

2 **self-compacting concrete based on uniaxial tension test**

3 Xing Li[a,b], Xudong Chen[a]*, Andrey P Jivkov[c], Jinhua Zhang [d]

4 [a]College of Civil and Transportation Engineering, Hohai University, Nanjing, 210098,
5 P.R. China

6 [b]College of Water Conservancy and Hydropower Engineering, Hohai University,
7 Nanjing, 210098, P.R. China

8 [c]Department of Mechanical, Aerospace and Civil Engineering, The University of
9 Manchester, Manchester, M13 9PL, UK

10 [d]School of Civil Engineering, Southeast University, Nanjing, 210096, P.R. China

11

12 **Abstract**: Rubberized concrete is a new type of building material intended to ultise

13 waste rubber with a potential for significant economic and environmental benefits.

14 However, its strength is lower than the strength of ordinary concrete due to the

15 introduction of rubber material, which might affect its application in practical

16 engineering. To improve the mechanical performance of rubberized self-compacting

17 concrete (RSCC), it is a necessary to study the internal mechanisms of strength

18 formation, degradation and failure. Based on the uniaxial tensile test of RSCC, this

19 work reports on the development and validation of a mesoscale model of RSCC, which

20 accounts for its heterogeneity. RSCC is considered to be composed of mortar, coarse

21 aggregate, rubber particles, aggregate-mortar interface transition zone (A-M ITZ),

22 rubber particle-mortar interface transition zone (R-M ITZ), and initial defects. The

23 mesoscopic model is validated by comparing the simulation results with test results.

*Corresponding author
E-mail: cxdong1985@hotmail.com

24   The model is then used to analyse the mechanical properties, crack generation and

25   propagation, and expansion of self-compacting concrete (SCC) and RSCC are

26   compared and analysed. Further, the effects of different volume fractions of rubber on

27   the mechanical properties of RSCC are studied. It is found that the mechanical

28   properties and final fracture surface morphology of RSCC with different rubber content

29   are significantly different, and the causes of these differences are discussed.

30   **Keywords:** RSCC；R-M ITZ；Uniaxial tensile test；3D mesoscale model；Fracture

31   property; Crack morphology

32   1. Introduction

33   Nowadays, waste rubber, predominantly from used tires, has become the second-largest

34   polymer pollutant and its disposal has attracted increasing attention across countries

35   and governments. The treatment of waste rubber generally included physical processing,

36   chemical decomposition, stacking, landfill, and combustion. Among these, landfill,

37   burning, and chemical decomposition are very harmful to the environment, and natural

38   placement cannot clear up the waste rubber for a short period. An effective method to

39   deal with the waste rubber is by crushing used tires and adding them into rubberized

40   concrete after physical processing. Rubberized concrete can effectively solve the

41   problem of disposal of rubber products such as used tires and has unique advantages in

42   environmental protection.

43   In the production process of rubberized concrete, rubber powder or rubber particles

44 are used to replace the coarse and fine aggregates inside the concrete by equal volume

45 or equal mass. The incorporation of rubber particles changes concrete properties from

46 the known properties of plain concrete. Eldin [1], Toutanji [2], Topcu [3], Guoqiang li

47 [4], F. Hernandez [5,6] demonstrated experimentally that with the increase of rubber

48 content, the compressive strength, flexural strength and tensile strength of concrete

49 specimens decreased, while plastic properties improved significantly. L.Zheng [7],

50 Feng Liu [8] studied the seismic performance of rubberized concrete by vibration test.

51 The test results showed that the damping ratio of rubber concrete was much higher than

52 the ordinary concrete, and the dynamic elastic modulus was lower than the ordinary

53 concrete. Wang her Yung [9] studied the durability of RSCC through experiments. The

54 results showed that the toughness and durability of RSCC could be significantly

55 improved when the rubber content was 5%. These scholars have made many

56 contributions to explore the property of rubberized concrete and expand the engineering

57 utilization of rubberized concrete. A common conclusion from their research is that the

58 incorporation of rubber can significantly improve the apparent density, durability, shock

59 absorption, impact resistance, heat insulation, sound insulation, and other properties of

60 concrete but at the same time its strength will decline substantially. To improve the

61 strength of rubberized concrete, the crack pattern and failure mechanism need to be

62 studied and understood in sufficient detail, e.g. via explicit representation of its

63 constituents using meso-scale models. However, little attention has been given to this

64 type of modelling of rubberized concrete[10]. One of the very few contributions is the

65   work by Feng Liu [11]   who considered the rubberized concrete as a composite of

66   aggregate, rubber and mortar, which however is quite different from the actual

67   rubberized concrete where interfacial transition zones(ITZs) are known to control

68   damage initiation and propagation. Another notable work is by ZH Xie [12], who

69   analysed the mechanical properties of rubberized concrete by a 2D model, where the

70   material contained four phases: aggregate, rubber, mortar, and aggregate-mortar

71   interface. This work, however, omitted explicit representation of the phase with weakest

72   mechanical properties, namely R-M ITZ. Furthermore, 2D analysis is not a reliable

73   approach to studying the complex crack patterns forming in real materials. To the best

74   of our knowledge, a study regarding rubberized concrete as a six-phases material

75   composed of aggregate, rubber, mortar, voids, A-M ITZ, R-M ITZ, in a 3D mesoscale

76   heterogeneous model has not been proposed to date. Such a study would allow for

77   substantially more realistic representation of the rubberized concrete mesostructure and

78   correspondingly more reliable analysis and discussion of its mechanical properties. In

79   this paper, appropriate 3D meso-scale model is proposed and validated using uniaxial

80   tensile tests. The model is used to investigate the crack formation mechanism and

81   mechanical properties of rubberized concrete.

82   The paper is organised as follows. Uniaxial tension tests of rubberized self-

83   compacting concrete with different rubber particle content are presented in Section 2.

84   Based on the test results, a 3D mesoscale model of rubberized self-compacting concrete

85   is established and presented in Section 3. The parameters and constitutive law of the

86   3D model are determined by the test results and trial calculations. Model validation is

87   performed in Section 4, where comparison between simulations and experiments is

88   shown. Section 5 presents parametric studies investigating the effects of rubber content

89   on the strength, crack initiation, crack propagation and fracture morphology. Both test

90   results and simulation results show that the toughness of RSCC is improved compared

91   with that of SCC without rubber particle. The incorporation of rubber particles reduces

92   the failure rate of the whole prism and controls the final fracture morphology of the

93   uniaxial tensile cracks of RSCC.

94   **2. Experiment programme**

95   **2.1 Materials**

96   The exact mix proportions of RSCC used in this paper are shown Table 1. The materials

97   used are listed as follows: P.O.42.5 plain Portland cement with a density of 2600

98   kg/m^3 ; gravel with size distribution shown in Table 2; river sand; rubber particles

99   with a density of 1050 kg/m^3 ; fly ash; silica fume; highly efficient polycarboxylate

100 water reducer; tap water. Fine rubber particles were produced by mechanical shredding

101 of waste tire. These particles were sieved, and the particles with a size ranging from

102 3~5mm retained. The fine aggregate of concrete is replaced by the sieved rubber

103 particles in the volume of 0%, 5%, 10%, and 15 %, respectively. The specimens with

104 fine aggregates was replaced with 0%, 5%, 10%, 15% rubber particles were designated

105 by RSCC-0, RSCC-5, RSCC-10 and RSCC15, respectively.

2.2 Specimen production

Prescribed amounts of material according to the mix proportion - fine aggregate, cement, fly ash and silica fume - were added and mixed for the 30s in the concrete mixer. This was followed by coarse aggregate addition and to thorough stirring. Finally, the tap water, water reducer and rubber particles were added and mixed for 3 minutes. The produced fresh concrete was discharged and poured into plastic molds with dimensions of $100mm \times 100mm \times 400mm$. The molds were removed after 24h. Then specimens were cured in water for 28 days. As mentioned before, four groups specimen with different rubber content were prepared.

2.3 Specimen processing

According to the previous studies [13,14], when the cross-section of a prism specimen is kept constant, the measured tensile strength of the prism decreases with the increasing of prism length of the prism due to size effect. However, when the aspect ratio of prismatic specimens is 3~4, the measured tensile strength tends to be a constant. At the same time, due to the clamping method used in this paper, the stress distribution in the test piece is very uniform for a specimen with a length greater than 200 mm. Thus, the length of the specimen was selected to be 300mm. Before the test, the specimens were taken out from the curing pool and their lengths reduced by cutting off 50mm from both ends. The specimens were cleaned up and steel plates with the same size were attached at both ends using adhesive glue. The tensile strength of the glue used is not less than

126   10MPa, which is higher than the tensile strength of the concrete specimen, ensuring that

127   it will not be degummed during the tensile test. The steel plate was connected to the

128   testing machine through the ball hinge, as shown in Fig. 1. The horizontal ruler was

129   used for calibration in the process of pasting the steel plate to avoid the influence of

130   eccentricity. The positioning hole on the pasted steel plate was located at the section

131   centroid of the specimen to ensure the geometric alignment of the tensile test.

132   **2.4 Experimental procedure**

133   A 500kN MTS322 electro-hydraulic servo testing machine was adapted for loading,

134   and the specimen was connected to the testing machine through ball hinge. The test

135   machine was equipped with an extensometer (standard gauge 280mm, measuring range

136   ±2.5mm), which could measure the deformation of the recorded test piece and could

137   also be used to control the test loading process. The extensor installation diagram is

138   shown in Fig. 1.

139   The deformation of the specimen was used as a control signal in the test loading to

140   obtain the full tensile stress-strain tensile curve. During the test, the load sensor of MTS

141   was used to measure the direct tension of the specimen, and the extensometer was

142   adopted to measure the deformation of the specimen.

3. 3D mesoscale model generation process and numerical simulation setup

3.1 CDP Constitutive model

Under the external load of the concrete, in addition to the stiffness degradation phenomenon caused by damage, unrecoverable permanent plastic deformation will also occur. In recent years, many researchers have applied the two theoretical frameworks of plasticity and damage to characterize the mechanical behavior of concrete, such as Grassl [15], Badel [16], and Kim et al. [17]. The plastic-damage model of concrete proposed by Lubliner et al. [18] and improved by Lee and Fenves [19] can not only characterize the permanent plastic deformation of concrete under external load but also describe the stiffness degradation caused by damage accumulation of concrete and the mechanical behavior of material softening after reaching peak strength. The main idea of the concrete damage model is to assume that the failure pattern of concrete is cracking during tension and crushing under compression. The isotropic damage variable is used to characterize the stiffness degradation and unrecoverable plasticity caused by a tensile fracture and compression failure of concrete. This is described mathematically by:

$$\sigma = (1 - D)D_0^{el} : (\varepsilon - \varepsilon^{pl}) \qquad (1)$$

where D represents the isotropic damage variable; D_0^{el} is the initial linear isotropic elastic modulus; ε^{pl} represents the plastic strain tensor. The evolution of plasticity is

163 described by two hardening parameters, $\tilde{\varepsilon}_t^{Pl}$ and $\tilde{\varepsilon}_c^{Pl}$, where footers "t" and "c"

164 respectively represent tension and compression. Figures 2 (a) and (b) respectively

165 show the mechanical behaviour of concrete under uniaxial compression and tension.

166 Under tension, the material is linear elastic before reaching its strength f_t, and the

167 stiffness degradation occurs after exceeding the tensile strength. The softening stress-

168 displacement relation characterizes the stiffness degradation behaviour. Under

169 compression, the material is linear elastic before reaching a yield strength, typically

170 40%~60% of the compressive strength. When the stress is larger than the yield stress

171 but less than the peak stress, the material is in a strain hardening regime. After

172 exceeding the compressive strength (peak stress), strain softening, and stiffness

173 degradation occur. Uniaxial tensile and compressive stress-strain relationships can be

174 described in the form of stress and plastic strain, as follows:

175 $$\sigma_t = \sigma_t\left(\tilde{\varepsilon}_t^{pl}, \dot{\tilde{\varepsilon}}_t^{pl}, \theta, f_i\right) \qquad (2a)$$

176 $$\sigma_c = \sigma_c\left(\tilde{\varepsilon}_c^{pl}, \dot{\tilde{\varepsilon}}_c^{pl}, \theta, f_i\right) \qquad (2b)$$

177 where $\dot{\tilde{\varepsilon}}_t^{pl}$ and $\dot{\tilde{\varepsilon}}_c^{pl}$ is the equivalent plasticity strain rate of tension and compression,

178 respectively; θ is temperature; f_i $(i = 1,2,\dots)$ is custom field variable.

179   Under uniaxial tension and compression, the stiffness degradation of concrete

180 materials is defined by two independent uniaxial damage variables, namely the tensile

181 damage factor d_t and the compression damage factor d_c. The stress-strain

182 relationship of the material under uniaxial tension and compression conditions

183 corresponds to Fig. 2, and the expressions are:

184
$$\sigma_t = (1 - d_t)E_0\big(\varepsilon_t - \tilde{\varepsilon}_t^{pl}\big) \qquad (3a)$$

185
$$\sigma_c = (1 - d_c)E_0\big(\varepsilon_c - \tilde{\varepsilon}_c^{pl}\big) \qquad (3b)$$

186   **3.2 Generation of RSCC 3D mesoscale model**

187   Since the study of RSCC mesoscale model is uncommon, this paper attempts to

188   simulate the RSCC uniaxial tension test with a 3D mesoscale model for the first time

189   and explores other mechanical properties of RSCC through the established model.

190   The difficulty in establishing the 3D mesoscale model is that due to the

191   incorporation of rubber particles, a transitional zone between the rubber and the mortar

192   will be formed which is similar to the interface between the mortar and the coarse

193   aggregate. The nature of the interface transition zone between mortar and aggregate has

194   always been a hot topic of scholars. Nowadays, many scholars [17,20–24] regard the

195   interface transition zone between mortar and aggregate as a material similar to mortar,

196   but its porosity is much higher than mortar. Due to the existence of natural defects such

197   as voids and pores, it has always been a weak area of the overall structure. According

198   to the research of [5], the thickness of R-M ITZ is around 60 microns. And the thickness

199   of A-M ITZ is about 10~50 microns [25–27]. Therefore, the thickness of the R-M ITZ

200   is similar to that of the A-M ITZ. During the process of simulation, the most common

201   way is to treat the A-M ITZ as a thin layer of a certain thickness outside the aggregate.

202   Most scholars believed that the thickness of the A-M ITZ is fixed [21,23,28,29], while

203   H. Chen [30] thought that the thickness of the A-M ITZ varies with the size of the

204 aggregate. The larger the aggregate size, the thicker the A-M ITZ. Since this paper aims

205 to explore the mesoscale model of RSCC, the influence of the ITZ on the properties of

206 the material is not the focus. Therefore, the thickness of A-M ITZ and R-M ITZ are all

207 taken as 0.25mm to facilitate mesh generation and simulation calculation. In this paper,

208 coarse aggregate and rubber are assumed to be linear elastic materials, while mortar, A-

209 M ITZ, and R-M ITZ are defined as plastic-damaged materials, which all obey the CDP

210 constitutive model described above albeit with different parameters [28,29].

211   Many scholars have explored the method of establishing the mesoscale concrete

212 model [31–34] and used a variety of ways to generate aggregate particles and voids in

213 the concrete matrix. Generally, there are two specific methods to build the mesoscopic

214 model, one is a synthetic parameterization method, and the other is an image-based

215 modelling method. In the first method, the particles are randomly placed in the space

216 according to a pre-arranged particle distribution. The limitation of this method is the

217 position and size distribution of the aggregate are different from the actual concrete

218 specimen. But it has the advantage of an easy implement. The most significant

219 advantage of the second method is that the model is generated by X-ray tomography

220 (XCT) 2D image, and the created model has the same mesostructure with the test

221 sample. This method can reconstruct a series of 2D images into a 3D structure, and

222 further mesh and rebuild them into finite element models. The most significant

223 disadvantage of the second method is time-consuming and expensive, and the

224 reconstructed finite element model tends to be unable to perform further numerical

225 simulation and analysis due to a large number of elements. In this paper, the synthetic

226 parameterization method is used to generate the model with insufficient aggregate and

227 rubber particle distribution information, and then the generated 3D mesostructure is

228 transformed into a pixel-based image. Finally, the finite element model is generated by

229 an image-based method. The shape of the particles in this paper is all spheres to simplify

230 the mesoscale model.

231   The aggregate in concrete can be divided into coarse aggregate and fine aggregate,

232 only coarse aggregate is considered in the model, and fine aggregate is composed of

233 mortar together with cement. The particle size distribution of the coarse aggregate in

234 the model is consistent with the experimental gradation setting, as shown in Table 2.

235 The rubber particles are also kept consistent with the experimental setup; all the rubber

236 particle size is in the range of 3~5mm. Pores and voids are weak areas of concrete, and

237 the presence of pores and voids can provide a channel for the development of cracks.

238 Therefore, to fully reflect the mesostructure of concrete, the pores and voids should also

239 be included in the mesoscopic model. According to the CT scan results [35], the pore

240 size range is 1~2mm, and the porosity of SCC is 1%~3%. So, in this paper, the porosity

241 of the mesoscale model is set as 1%. Similarly to Ref.   [24], finite-thickness A-M ITZ

242 and R-M ITZ elements are generated by enlarging aggregates and rubber particles

243 before the model is tessellated into voxels. Enlargement by radius increment of 0.25

244 mm is used for A-M ITZ and R-M ITZ.

245   The critical technology for model generation is the need to repeatedly generate

246   aggregates, rubber particles, and voids until the content of these three components

247   reaches a predetermined volume fraction. The whole process of particle filling consists

248   of three procedures: input- taking- placing. The input procedure is to input the dominant

249   information to generate randomly distributed aggregate, rubber particles, and voids

250   structure. The taking process produces aggregates, rubber particles, and pores

251   consistent with the random size and distribution demand. All the generated particles are

252   then placed into pre-defined areas irregularly and randomly according to pre-set

253   physical boundaries of the specimen. When placing particles into a given area, the

254   essential principle is that the aggregate, rubber particles, and pores cannot intersect or

255   overlap. In this paper, a direct, effective and easy method to implement 3D spherical

256   overlap detection is proposed which can be easily fulfilled by meeting the following

257   three requirements: (1) each particle must be contained within the volume of the

258   concrete, which can be satisfied by controlling the maximum and minimum values of

259   the particle coordinates; (2) there is no overlapping and intersect between all particles;

260   (3) the distance between all particles and the boundary of the concrete specimen should

261   be within a specific range, and the particles do not intersect with the concrete boundary.

262   As shown in Equation (4), for two sphere particles, the intersection and overlap

263   conditions can be easily checked by comparing the particle centre distance and the sum

264   of the two radii.

265
$$\sqrt{(x_0' - x_0)^2 + (y_0' - y_0)^2 + (z_0' - z_0)^2} \leq r + r' \qquad （4）$$

266   x_0 , y_0 , z_0 are the center coordinates of the existed sphere, r is the radius of the sphere,

267　x_0', y_0', z_0' are the center coordinates of the newly generated sphere, and r' is the

268　radius of the newly generated sphere.

269　　　Based on the above algorithm, a MATLAB code is compiled to generate concrete

270　specimens with randomly distributed aggregates, rubber particles, and voids. The flow

271　chart of the code to generate random particles is shown in Fig. 3.

272　　　To reduce the number of three-dimensional model elements and improve the

273　computational efficiency, the size of the 3D model specimens was set as

274　$50mm \times 50mm \times 150mm$, half of the test specimens. In this paper, four groups of

275　mesoscale numerical models were generated with the same composition and particle

276　gradation as in the test specimens. As shown in Fig. 4, the aggregate and rubber content

277　of the mesoscale model is the same in the test specimen.

278　**3.3 Uniaxial tensile simulation of the concrete prism**

279　The uniaxial tensile test of the concrete prism is conducted by the electro-hydraulic

280　servo tester simultaneously applies a tension force to the specimen at both ends

281　through a ball hinge. In the numerical simulation, to obtain the stress-strain

282　relationship from the simulation results, the specimen was fixed at one end, and the

283　displacement load was applied on all nodes at the other end. The solution was

284　obtained through the standard analysis of Abaqus. The simulation parameters used in

285　this paper are shown in Table 3. Similar to previous works [13,15,21,31–33], it is

286　assumed that the aggregate is linear elastic material which will not be damaged, and

287   the crack will not develop inside the aggregate. The rubber is originally an elastic

288   material, and its material parameters maintain its inherent material properties. The

289   selection of mortar parameters is inferred from the test results of SCC without adding

290   rubber. The study on the R-M ITZ parameters is not so common, but the study of [5]

291   shows the porosity of the R-M ITZ is quite larger than that of the A-M ITZ, and the

292   microstructure is worse than that of the A-M ITZ.   It can be inferred that the

293   mechanical properties of the R-M ITZ are worse than the A-M ITZ. The parameters of

294   the A-M ITZ and the parameters of the R-M ITZ are obtained by referring to the

295   parameters in literature [11,12,15,24,33] and through trial calculation. The rationality

296   of the parameters used in this paper is verified by comparing the test and the

297   simulation results in section 4.

298   4. Comparison of test results with numerical simulation results

299   One of the RSCC-0 tensile tests failed during the testing process, so there was only

300   one effective test result of the RSCC-0 specimen. All the other specimen group has

301   two sets of test results, which can be used for validation. To prevent the low reliability

302   of simulation results caused by the difference in composition and the random

303   distribution of aggregate and rubber particle of a single model, three random

304   mesoscale models of each component were selected for numerical simulation. The

305   comparison of numerical simulation results and test results of each specimen group is

306   shown in Fig. 5, and the crack pattern and location of the test specimen and simulation

307   specimen are shown in Fig. 6.

308   As can be seen from Fig. 5, the consistency between the simulated result and the

309   test result is very high before the peak stress, indicating that the selected elastic modulus

310   is appropriate. The uniaxial tensile strength of the numerical simulation results is

311   basically within the range of the two groups of tests results. Moreover, the dispersion

312   of the uniaxial tensile strength of the three random mesoscale models is minimal,

313   indicating that the numerical model has a superior performance for predicting the

314   uniaxial tensile strength. The concrete specimen is damaged quickly after the peak

315   stress, and the strength decreases rapidly, but due to the diverse distribution of aggregate

316   and rubber particles, the difference between the mesoscale model and actual

317   components of the concrete prism, the simulation results of the post-peak period has

318   slight difference with the test results. It can also be seen from the test curves of Fig. 5

319   (b), (c) and (d) that due to the different internal composition and aggregate, rubber

320   particle distribution, the test results of two concrete specimens of the same component

321   also have dispersion in the post-peak section. After reaching the ultimate strength, the

322   micro-cracks in the concrete gather rapidly, nucleation, develop into macroscopic

323   cracks, and eventually lead to the final failure of the whole structure. The development

324   of cracks is closely related to the distribution of aggregates, rubber particles, defects

325   and voids of the specimen itself. The existence of defects and voids can provide a

326   development channel for cracks and promote its development rate. So the stress-strain

327   response after the peak stress of different specimen will be different, but the overall

328   development trend of the stress-strain curve is similar.   In conclusion, the proposed

329 3D mesoscale model can reflect the properties and the overall performance of RSCC;

330 the simulation elastic modulus is very consistent with the elastic modulus of the

331 material itself; the material strength floats in a certain error range. The material

332 performance of the post-peak section has slight discrepancy due to the different

333 components and aggregate distribution of the specimen. The global trend of the stress-

334 strain curve is consistent with the test results, which shows that the proposed 3D

335 mesoscale model in this paper can produce the overall performance of RSCC and

336 verified the feasibility of the proposed model. As can be seen from Fig. 6, the position

337 and morphology of the cracks in the numerical simulation results are very close to the

338 experimental results, which supports that the 3D mesoscale simulation results are

339 reasonable and reliable.

340 **5. Discussion**

341 **5.1 Effect of rubber content on the tensile strength of RSCC**

342   Figure 7 shows all the test results of RSCC under uniaxial tension. A conclusion

343   can be drawn from the figure that as the rubber content increases, the peak stress of

344   the specimen decreases, while the strain corresponds to the peak stress of the

345   specimen increases, indicating that with the increase of rubber content, the material

346   strength decreases, and toughness slightly increases. Due to the test conditions, the

347   environment influence, and the different structure of each specimen, the test results

348   have a certain degree of dispersion. From Fig. 6, the numerical simulation results

349   of the RSCC of each component have a small dispersion and maintain a high degree

350   consistent with the test results. A numerical simulation result was randomly selected

351   from each group of all the simulation results and plotted in Fig. 8 (a) to facilitate

352   the discussion and analysis of the simulation results. It can be seen in Fig. 8(a) that

353   the elastic modulus of the material decreases with the increase of rubber content

354   before the peak stress. The material strength decreases clearly with the increase of

355   rubber content, while the corresponding peak strain increases, and the material

356   toughness increases. With the increase of rubber content, the failure speed of the

357   material decreased during the post-peak period. The strength of the RSCC is

358   decreased, and the peak strain is significantly improved as compared with the

359   reference SCC (concrete without rubber particles). For all RSCC specimens, the

360   strength of the specimen decreases as the rubber content increases, and the peak

361   strain increases as the rubber particle content increases. The reason for the above

362   test and simulation results is that the addition of rubber particles in the concrete can

363   increase the toughness of the concrete but reduce the strength simultaneously. The

364   reason for the toughness enhancement of concrete is that the size of rubber particles

365   is small, which can fill the defects and voids of concrete. Besides, the rubber

366   particles can also play a role in optimizing the gradation of fine aggregate and coarse

367   aggregate. The elastic modulus of rubber is smaller than all the other components;

368   rubber can effectively relieve the stress concentration at the tip of the crack, thus

369   slowing down the expansion of cracks and enhancing the toughness of concrete

370　　during the process of loading. Besides, the incorporation of rubber particles is

371　　equivalent to introducing new initial defects into the concrete due to the small

372　　elastic modulus of rubber. Rubber belongs to the organic materials; the concrete

373　　belongs to the inorganic materials. The different material type makes the cohesion

374　　at the interface transition zone between rubber and mortar weaker. The rubber

375　　particle can also play the role of air-entraining agent; the addition of rubber particle

376　　will increase the gas content in concrete. With the increase of rubber content, the

377　　concrete porosity increases, resulting in the reduction of the overall strength of the

378　　material.

379　　**5.2 Effect of rubber content on crack development**

380　　**5.2.1 Analysis of microcrack development**

381　　Due to the limitation of test detection technology, it is impossible to observe and

382　　analyze the development of internal cracks of concrete in the process of tensile

383　　failure. Therefore, the development process of internal cracks of concrete is

384　　compared and analyzed using mesoscale simulation technology. After verifying the

385　　reliability of the simulation results through the comparison between the above test

386　　results and the simulation results, the simulated specimens which are consistent

387　　with the specimen setting and have good crack morphology development are

388　　selected for comparative analysis on the development of micro-cracks. Figures 9,

389　　10, 11, and 12 show the development and distribution of microcracks in the four

390   specimen types. The points in Figures. 9 (a), 10 (a), 11 (a) and 12 (a) mark the same

391   loading times for the four different models under uniaxial tension. Figures 10 (a),

392   11 (a) and 12 (a) have one additional point, p_0, compared with Figure. 9(a). This is

393   the point where microcracks appear in specimens containing rubber, while no

394   microcracks that can be seen by the naked eye at the same loading time in ordinary

395   SCC. This is further demonstrated in Figs. 9 (b), 10 (b), 11 (b) and 12 (b), where

396   microcracks of RSCC appear earlier than the SCC specimen under the same load.

397   The green and red parts in these figures represent increasing degree of damage, i.e.

398   microcrack generation. Additionally, it is shown that the number of microcracks in

399   RSCC specimen is great than that of SCC specimen, and the degree of damage in

400   RSCC is larger at the same loading time point.

401   During the initial stage, shown by points p_1, p_2, p_3 in Figs. 9 (b), 10 (b), 11 (b)

402   and 12 (b), microcracks appear in the weakest parts of the specimens – the ITZs.

403   With microcracks extension and coalescence one of these develops into the main

404   crack, which eventually leads to destruction of the specimen. It can be seen from

405   the figures that the concrete specimen is not destroyed immediately after the peak

406   stress, as the internal cracks are still in the microcrack stage, a macrocrack has not

407   been formed yet. This illustrates that concrete is a quasi-brittle heterogeneous

408   material, not an entirely brittle material, where its microstructure controls the

409   development of cracks. After reaching the tensile strength, the development of

410   internal cracks is intensified and aggravated, and the material performance

411   significantly declines, underpinned by the formation of macrocracks. After this

412   point, the energy required for crack development is much less than the energy

413   required for crack propagation before the peak stress. Comparing Fig. 9 (b) and Fig.

414   10 (b), it is seen that time for microcracks generation in RSCC specimen is less than

415   in the ordinary SCC before the peak stress, and the microcrack development in

416   RSCC before the peak stress is faster. This shows that the incorporation of rubber

417   particles increases the overall defects in the structure and weakens the material

418   performance of the pre-peak phase, which also supports the conclusion in section

419   5.1. In the initial phase, microcracks appear throughout the specimen, not just

420   located at the position which will lead to macrocrack and the final failure of the

421   specimen. The macrocrack location is closely related to the spatial distribution of

422   the concrete components as suggested by the crack location in Figs. 10 (b), 11 (b)

423   and 12 (b); different realisation of the randomly distributed components will result

424   in a different crack pattern.

425   **5.2.2 Effect of rubber content on the development of macroscopic cracks**

426   Based on the analysis of 5.2.1, this section selects RSCC-0 and RSCC-15 specimen to

427   conduct a comparative analysis on the development process of macroscopic cracks to

428   further analyse the influence of rubber incorporation on the development of

429   macrocracks in concrete. The crack development after the peak stress of the selected

430   mesoscale specimen, corresponding to time points of $s_1 \sim s_4$, is shown in Figs. 9 (c) and

431   12 (c). As can be seen from these figures, the rate of macrocrack propagation after the

432   peak stress is higher in RSCC-0 than in RSCC-15. The microcracks in RSCC-0

433   specimens have been clustered into nuclei at the time s_1 after the peak, while the

434   microcracks in RSCC-15 are more dispersed at the same time. At the moment s_4, the

435   concentrated internal damage in specimen RSCC-0 is very high and the overall failure

436   of the material is observed, while the concentrated internal damage in specimen RSCC-

437   15 is lower, indicating that the addition of rubber improves the overall toughness of the

438   material and reduces the rate of macrocrack propagation.

439   **5.3 Effect of rubber content on crack morphology**

440   Figure 13 shows the morphology of the final failure surfaces for the four specimen types.

441   As can be seen in Fig. 13(a), the crack in RSCC-0 mainly occurs at the transition

442   interface between aggregate and mortar. During the crack development process, some

443   big voids will appear in the crack surface, as the crack avoids aggregates which cannot

444   be damaged. The number of such voids in Figs. 13 (b), (c) and (d) is significantly

445   smaller, indicating that the addition of rubber optimizes the gradation of concrete

446   aggregate, and the area of the interface transition zone is significantly increased. As can

447   be seen from Figs. 13(b), (c), (d), the number of large voids in the whole crack surface

448   of the specimen decreases, and more small size voids appear with the increase of rubber

449   content. This is due to the increase of the number of rubber particles, which enables the

450   crack to develop and extend at both A-M ITZ and R-M ITZ. The size decrease of the

451   voids indicates that the crack will preferentially develop at the R-M ITZ, and the smaller

452   size rubber particles can be easily bypassed. At the same time, because of the size of

453   the rubber particle is smaller, the energy needed to bypass a rubber particle is much

454   lower than a bigger size aggregate. Therefore, the crack surface will produce some

455   smaller size voids when the specimen contains many rubber particles. The final crack

456   pattern also conforms to the hypothesis and setting of the mechanical parameters of the

457   material. Rubber particles and coarse aggregate are linear elastic materials, which will

458   not be damaged. Elastoplastic damage can occur in the mortar, A-M ITZ, and R-M ITZ.

459   The mechanical properties of A-M ITZ and R-M ITZ are inferior to mortar, so the

460   cracks mainly occur in these two areas. Since rubber is an organic material and mortar

461   is an inorganic material, the mechanical properties of the interface transition zone

462   between two different types of materials are inferior to the interface transition zone

463   between the same type of material. And it is known that the porosity of R-M ITZ is

464   significantly higher than that of A-M ITZ [4]. It is further known that the strength of

465   mortar materials is closely related to the porosity [36,37]. When the porosity is high,

466   the material strength is low, and when the porosity is low, the material strength is high.

467   Therefore, the interfacial transition zone between rubber and mortar is the weakest

468   interface in the material; the crack will preferentially develop at the R-M ITZ, followed

469   by the A-M ITZ.

470   **6. Conclusions**

471   Based on uniaxial tension test results of rubberized concrete, this paper explores the

472   application of mesoscale modelling to improve understanding of damage and failure of

473   such materials in view of their potential for economic and environmental benefits. The

474   following conclusions can be drawn from the work:

475   1. By comparing test and numerical simulation results for stress-strain response and

476   crack pattern and location, it is demonstrated that the proposed 3D mesoscale model

477   can be used to analyse damage evolution and crack development in RSCC. In addition,

478   the mesoscale model has the potential to be used in analysis of other mechanical

479   properties of RSCC.

480   2. The results of the RSCC prism test and numerical simulation show that the

481   toughness of RSCC is improved compared with that of SCC, and the bearing capacity

482   is reduced. When the rubber particle gradation is the same, with the increase of rubber

483   content, the strength of the specimen decreases, the toughness of the specimen increases,

484   and the overall damage rate of the material is reduced.

485   3. The final morphology of the uniaxial tensile cracks of RSCC shows that the

486   incorporation of rubber particle reduces the failure rate. Due to the incorporation of

487   rubber particles, the pores and defects of the concrete are filled, the gradation of the

488   concrete sand and aggregate is optimized, and the porosity of the test piece is reduced

489   to some extent. However, the total area of the interfacial transition zone is increased

490   significantly. The special properties of rubber materials lead to extremely high

491   interfacial porosity between rubber particles and mortar. The porosity brought by the

492   increased interfacial transition zone is much higher than that reduced by the

493   optimization of particle grading, so the overall strength of the material will still decline.

494   4. The R-M ITZ is the weakest constituent of rubberized concrete due to high porosity

495   and weak cohesion between two different types of material. Microcracks are easy to

496   nucleate and grow in this region, and eventually develop into macrocracks resulting in

497   the overall failure of the material.

Acknowledgments

501   **Reference**

502   [1]   E.N. N., S.A. B., Rubber-Tire Particles as Concrete Aggregate, J. Mater. Civ.

503   Eng. 5 (1993) 478–496. doi:10.1061/(ASCE)0899-1561(1993)5:4(478).

504   [2]   H.A. Toutanji, The use of rubber tire particles in concrete to replace mineral

505   aggregates, Cem. Concr. Compos. 18 (1996) 135–139.

506   [3]   İ.B. Topcu, Assessment of the brittleness index of rubberized concretes, Cem.

507   Concr. Res. 27 (1997) 177–183.

508   [4]   G. Li, M.A. Stubblefield, G. Garrick, J. Eggers, C. Abadie, B. Huang,

509   Development of waste tire modified concrete, Cem. Concr. Res. 34 (2004)

510   2283–2289.

511   [5]   F. Hernandez-Olivares, G. Barluenga, M. Bollati, B. Witoszek, Static and

512   dynamic behaviour of recycled tyre rubber-filled concrete, Cem. Concr. Res.

513   32 (2002) 1587–1596.

514   [6]   F. Hernández-Olivares, G. Barluenga, B. Parga-Landa, M. Bollati, B.

515   Witoszek, Fatigue behaviour of recycled tyre rubber-filled concrete and its

516   implications in the design of rigid pavements, Constr. Build. Mater. 21 (2007)

517   1918–1927.

518   [7]   L. Zheng, X.S. Huo, Y. Yuan, Experimental investigation on dynamic

519   properties of rubberized concrete, Constr. Build. Mater. 22 (2008) 939–947.

520   [8]   F. Liu, G. Chen, L. Li, Y. Guo, Study of impact performance of rubber

521   reinforced concrete, Constr. Build. Mater. 36 (2012) 604–616.

522   [9]   W.H. Yung, L.C. Yung, L.H. Hua, A study of the durability properties of waste

523   tire rubber applied to self-compacting concrete, Constr. Build. Mater. 41 (2013)

524   665–672.

525   [10]   O. Youssf, J.E. Mills, R. Hassanli, Assessment of the mechanical performance

526   of crumb rubber concrete, Constr. Build. Mater. 125 (2016) 175–183.

527   [11]   F. Liu, G. Zhong, X. Xia, L. Li, Mechanical analysis of rubberized concrete

528   subjected to uniaxial compression on meso-level, J. Build. Mater. 13 (2010)

529   733–738.

530   [12]   Z.H. Xie, Y.C. Guo, Q.Z. Yuan, P.Y. Huang, Mesoscopic numerical

531   computation of compressive strength and damage mechanism of rubber

532   concrete, Adv. Mater. Sci. Eng. 2015 (2015).

533   [13]   P. Grassl, D. Grégoire, L.R. Solano, G. Pijaudier-Cabot, Meso-scale modelling

534   of the size effect on the fracture process zone of concrete, Int. J. Solids Struct.

535   49 (2012) 1818–1827.

536   [14]   S.Y. Alam, P. Kotronis, A. Loukili, Crack propagation and size effect in

537   concrete using a non-local damage model, Eng. Fract. Mech. 109 (2013) 246–

538   261.

539   [15]   P. Grassl, M. Jirásek, Damage-plastic model for concrete failure, Int. J. Solids

540   Struct. 43 (2006) 7166–7196.

541   [16]   P. Badel, V. Godard, J.-B. Leblond, Application of some anisotropic damage

542   model to the prediction of the failure of some complex industrial concrete

543   structure, Int. J. Solids Struct. 44 (2007) 5848–5874.

544   [17]   S.-M. Kim, R.K.A. Al-Rub, Meso-scale computational modeling of the plastic-

545   damage response of cementitious composites, Cem. Concr. Res. 41 (2011)

546   339–358.

547   [18]   J. Lubliner, J. Oliver, S. Oller, E. Oñate, A plastic-damage model for concrete,

548   Int. J. Solids Struct. 25 (1989) 299–326.

549   [19]   J. Lee, G.L. Fenves, Plastic-damage model for cyclic loading of concrete

550   structures, J. Eng. Mech. 124 (1998) 892–900.

551   [20]   W. Tian, F. Dang, Y. Xie, Quantitative study on crack of meso-damage and

552   fracture concrete based on CT technique, Sadhana. 40 (2015) 263–276.

553   [21]   X.Q. Zhou, H. Hao, Modelling of compressive behaviour of concrete-like

554   materials at high strain rate, Int. J. Solids Struct. 45 (2008) 4648–4661.

555   [22]   R.R. Pedersen, A. Simone, L.J. Sluys, Mesoscopic modeling and simulation of

556   the dynamic tensile behavior of concrete, Cem. Concr. Res. 50 (2013) 74–87.

557   [23]   Z. Tu, Y. Lu, Mesoscale modelling of concrete for static and dynamic response

558   analysis-Part 1: model development and implementation, Struct. Eng. Mech. 37

559   (2011) 197–213.

560   [24]   Y. Huang, Z. Yang, W. Ren, G. Liu, C. Zhang, 3D meso-scale fracture

561   modelling and validation of concrete based on in-situ X-ray Computed

562   Tomography images using damage plasticity model, Int. J. Solids Struct.

563   (2015). doi:10.1016/j.ijsolstr.2015.05.002.

564   [25]   B.D. Barnes, S. DIAMOND, W.L. Dolch, Micromorphology of the interfacial

565   zone around aggregates in Portland cement mortar, J. Am. Ceram. Soc. 62

566   (1979) 21–24.

567   [26]   E.J. Garboczi, D.P. Bentz, Analytical formulas for interfacial transition zone

568   properties, Adv. Cem. Based Mater. 6 (1997) 99–108.

569   [27]   J.G.M. Van Mier, M.R.A. van Vliet, T.K. Wang, Fracture mechanisms in

570   particle composites: statistical aspects in lattice type analysis, Mech. Mater. 34

571   (2002) 705–724.

572   [28]   X.Q. Zhou, H. Hao, Mesoscale modelling of concrete tensile failure mechanism

573   at high strain rates, Comput. Struct. 86 (2008) 2013–2026.

574   [29]   Y. Lu, Z. Song, Z. Tu, Analysis of dynamic response of concrete using a

575   mesoscale model incorporating 3D effects, Int. J. Prot. Struct. 1 (2010) 197–

576   217.

577   [30]   H. Chen, B. Xu, Y.L. Mo, T. Zhou, Behavior of meso-scale heterogeneous

578   concrete under uniaxial tensile and compressive loadings, Constr. Build. Mater.

579   178 (2018) 418–431.

580   [31]   J.G.M. Van Mier, M.R.A. Van Vliet, Influence of microstructure of concrete on

581   size/scale effects in tensile fracture, Eng. Fract. Mech. 70 (2003) 2281–2306.

582   [32]   A. Caballero, C.M. López, I. Carol, 3D meso-structural analysis of concrete

583   specimens under uniaxial tension, Comput. Methods Appl. Mech. Eng. 195

584   (2006) 7182–7195.

585   [33]   X. Wang, M. Zhang, A.P. Jivkov, Computational technology for analysis of 3D

586   meso-structure effects on damage and failure of concrete, Int. J. Solids Struct.

587   80 (2016) 310–333.

588   [34]   Z. Yang, W. Ren, M. Mostafavi, S.A. Mcdonald, T.J. Marrow, Characterisation

589   of 3D fracture evolution in concrete using in-situ X-ray computed tomography

590   testing and digital volume correlation, in: VIII Int. Conf. Fract. Mech. Concr.

591   Concr. Struct., Toledo, Spain CIMNE, 2013: pp. 1–7.

592   [35]   Y. Huang, Z. Yang, W. Ren, G. Liu, C. Zhang, 3D meso-scale fracture

593   modelling and validation of concrete based on in-situ X-ray Computed

594   Tomography images using damage plasticity model, Int. J. Solids Struct. 67

595   (2015) 340–352.

596   [36]   X. Chen, S. Wu, J. Zhou, Influence of porosity on compressive and tensile

597   strength of cement mortar, Constr. Build. Mater. 40 (2013) 869–874.

598   [37]   Y. Wu, X. Zhou, Y. Gao, L. Zhang, J. Yang, Effect of soil variability on

599   bearing capacity accounting for non-stationary characteristics of undrained

600   shear strength, Comput. Geotech. 110 (2019) 199–210.

601

602

List of figure captions

603

604   **Fig. 1.** Test device and specimen

605   **Fig. 2.** The uniaxial stress-strain curve with damage plasticity

606   **Fig. 3.** Flowchart of random aggregates, rubber particles and voids generation

607   **Fig. 4.** Concrete mesoscale models with different compositions

608   **Fig. 5.** Stress-strain curve of each group RSCC specimen under uniaxial tension

609   **Fig. 6.** Crack pattern and location of each group RSCC specimen under uniaxial tension

610   **Fig. 7.** Stress-strain curve of RSCC under tension test

611   **Fig. 8.** Simulation result of RSCC with different rubber content under uniaxial tension

612   **Fig.9.** Simulation result of RSCC-0 specimen under uniaxial tension

613   **Fig.10.** Simulation result of RSCC-5 specimen under uniaxial tension

614   **Fig.11.** Simulation result of RSCC-10 specimen under uniaxial tension

615   **Fig.12.** Simulation result of RSCC-15 specimen under uniaxial tension

616   **Fig. 13.** Final crack morphology of RSCC specimens with different rubber content

List of table captions

622

Table 1 The mix proportion of RSCC (kg/m^3)

Specimen	Cement	Fly ash	Silica Fume	Water	Water Reducer	Rubber particle	Sand	Gravel
RSCC-0	385	139	26	200	7.5	0	1080	800
RSCC-5	385	139	26	200	7.5	52	1080	672
RSCC-10	385	139	26	200	7.5	104	1080	542
RSCC-15	385	139	26	200	7.5	156.5	1080	413

623

624

Table 2 Coarse aggregate size distribution

Sieve size (mm)	Total passed percentage (%)
10	100%
8	60%
6	0

625

626

627

Fig. 1. Test device and specimen

628
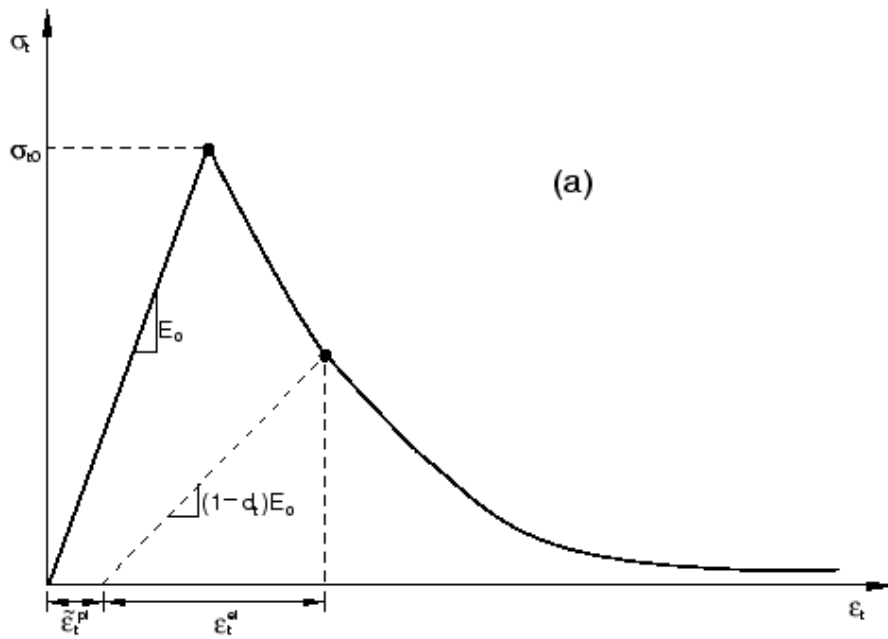
629

630   (a) Concrete response under uniaxial tension
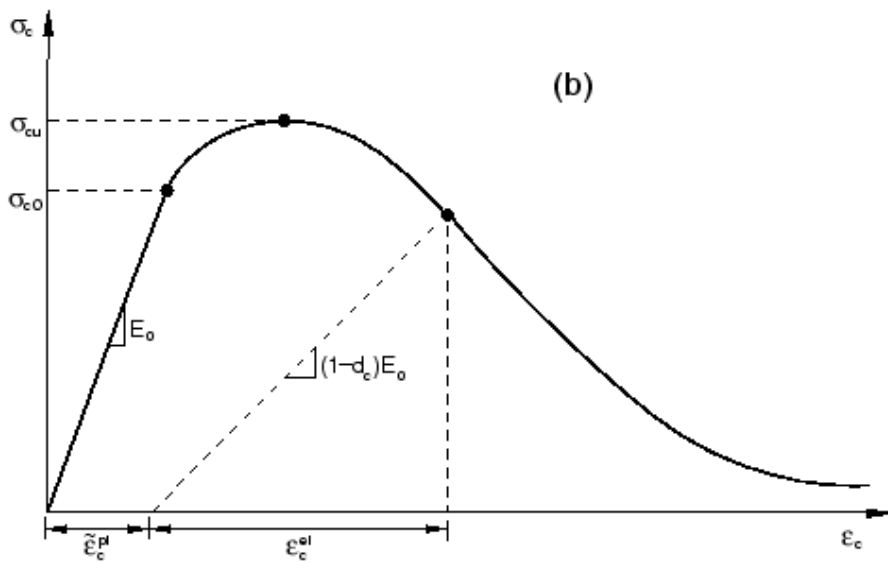
631

632   (b) Concrete response under uniaxial compression

633   **Fig. 2.** The uniaxial stress-strain curve with damage plasticity

634
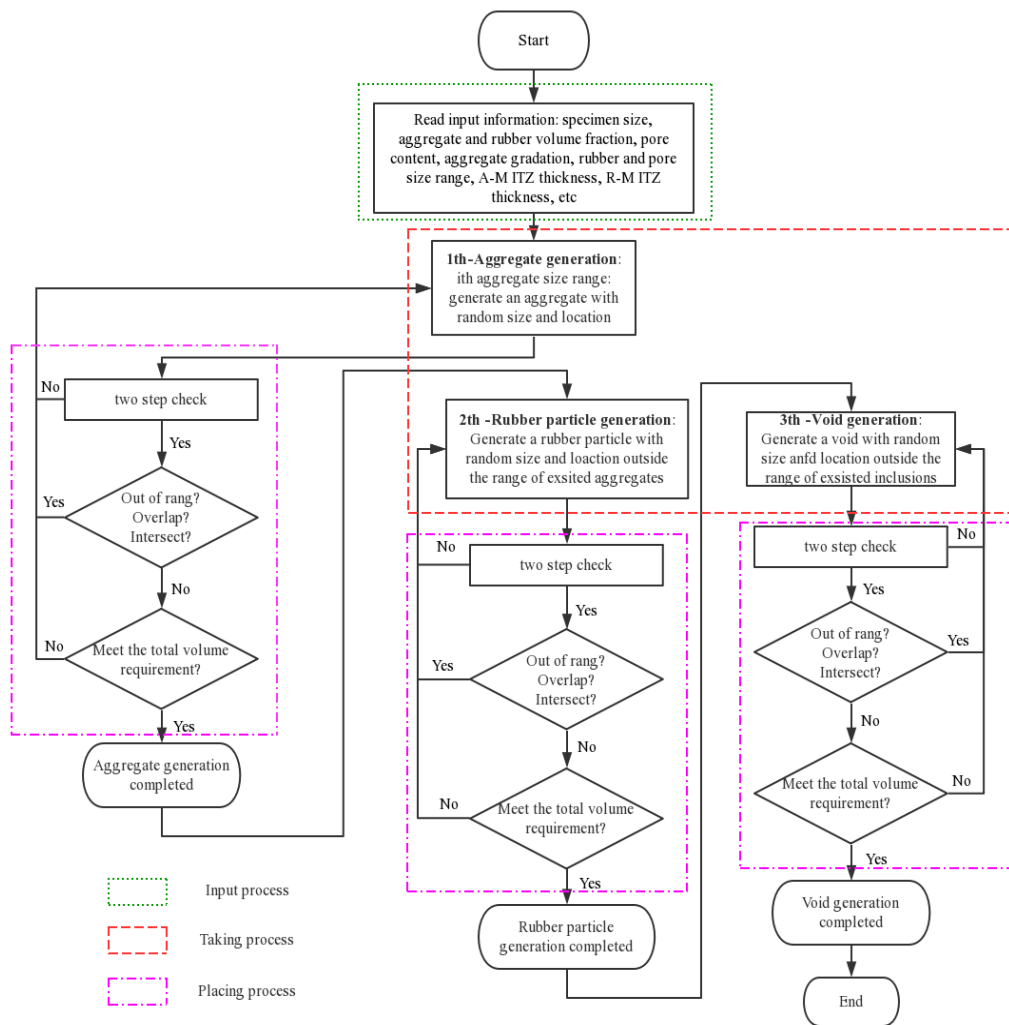
635

636   **Fig. 3.** Flowchart of random aggregates, rubber particles and voids generation

637

638
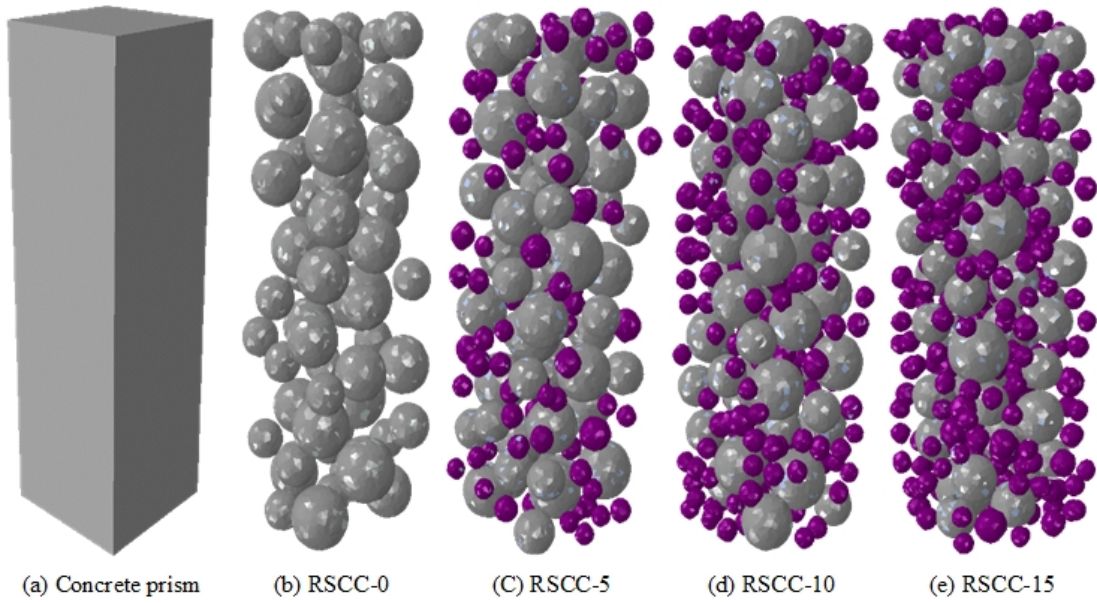
639   **Fig. 4.** Concrete mesoscale models with different compositions. Gray spheres are coarse

640   aggregate, and purple spheres are rubber particles

641

Table 3 Material parameters for RSCC meso-scale model

	Tensile strength (MPa)	Compressive strength (MPa)	Young's modulus (GPa)	Poisson's ratio	Density (Kg/m^3)
Mortar	4.4	60	42	0.2	2200
Coarse aggregate	--	--	40	0.2	2600
Rubber particle	--	--	7	0.4	1050
A-M ITZ	3	45	21	0.2	1800
R-M ITZ	1.5	25	12.5	0.2	1500

643

644

645
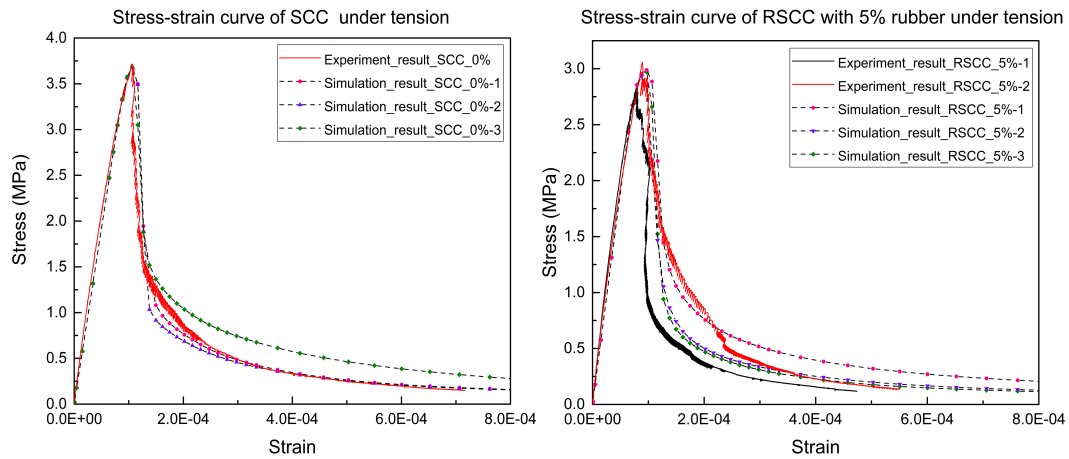
(a) Stress-strain curve of RSCC-0

(b) Stress-strain curve of RSCC-5
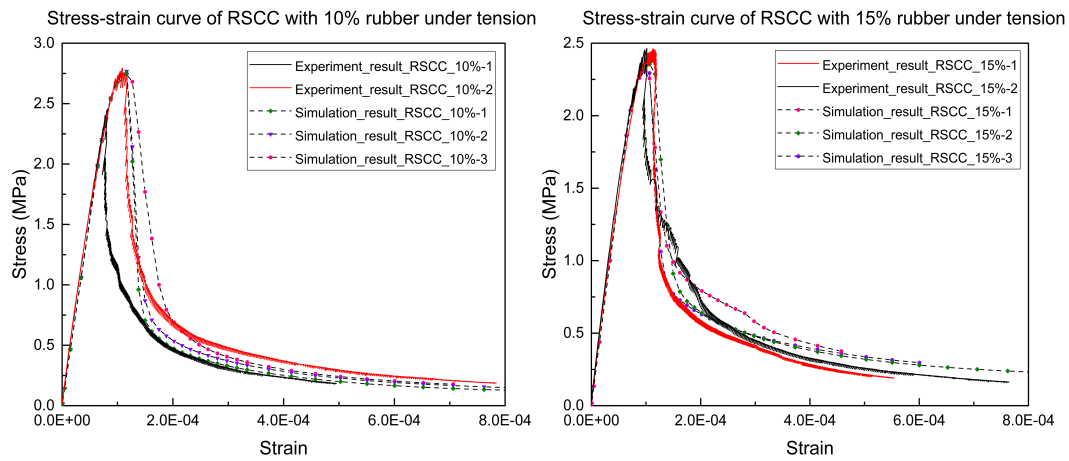
(c) Stress-strain curve of RSCC-10

(d) Stress-strain curve of RSCC-15

Fig. 5. Stress-strain curve of each group RSCC specimen under uniaxial tension

646

647

648

649

650

651
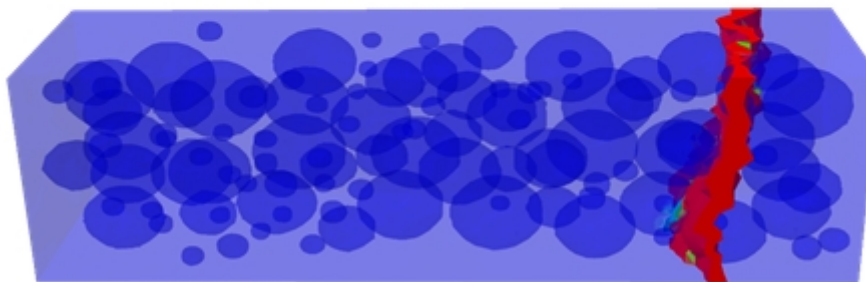
(a) RSCC-0 specimen with no rubber particle content

652
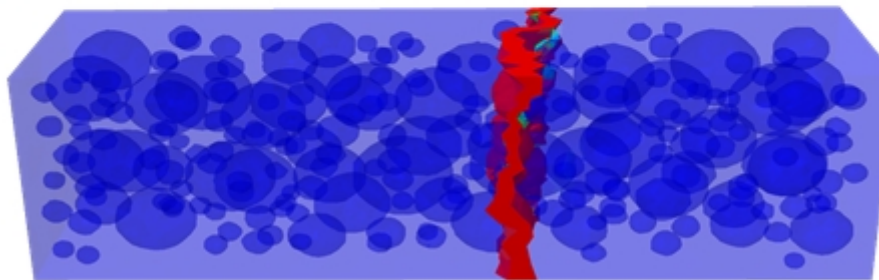
(b) RSCC-5 specimen with 5% rubber particle content

653
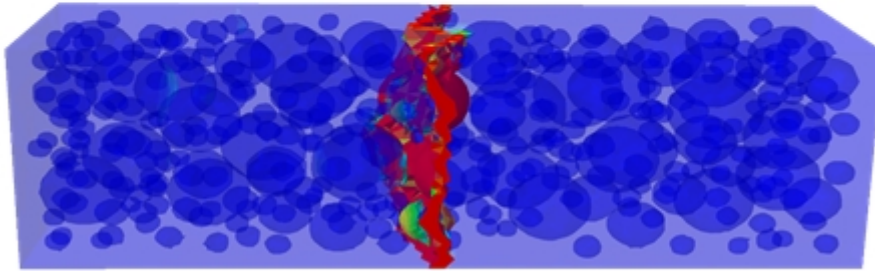
(c) RSCC-10 specimen with 10% rubber particle content

654
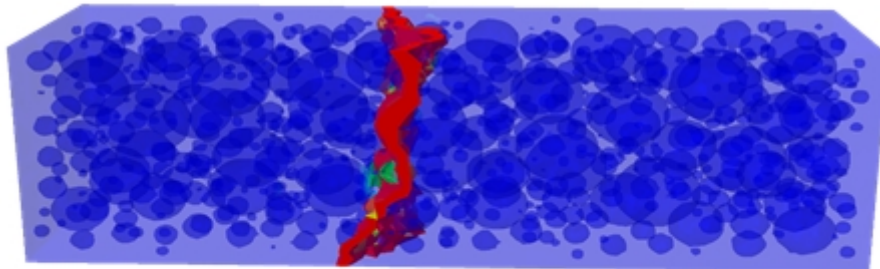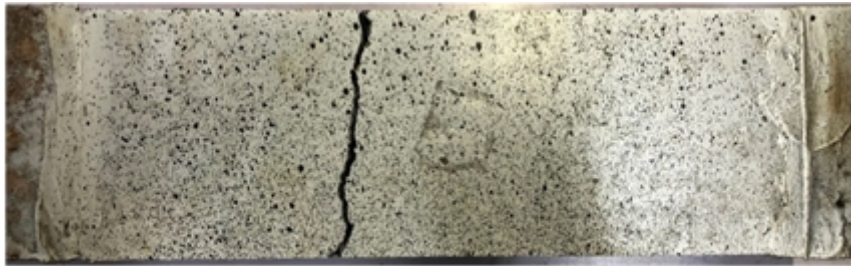
(d) RSCC-15 specimen with 15% rubber particle content

655

656   **Fig. 6.** Crack pattern and location of each group RSCC specimen under uniaxial tension

657

Experiment result of concrete specimen with different content
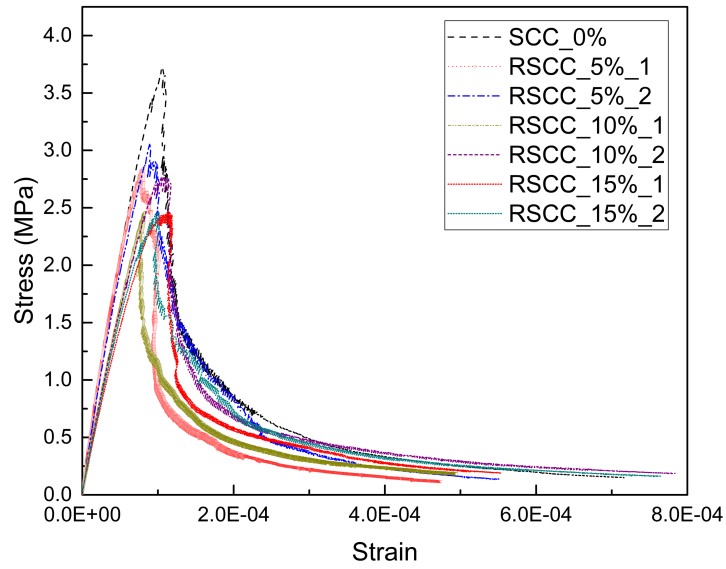
658

659   **Fig. 7.** Stress-strain curve of RSCC under tension test

Simulation result with different rubber content
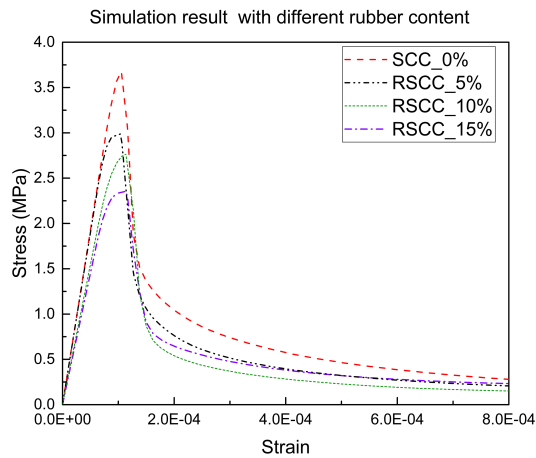
660

661   (a) Stress-strain curve of RSCC under tension simulation

Strength of mesoscale RSCC specimen with different rubber content
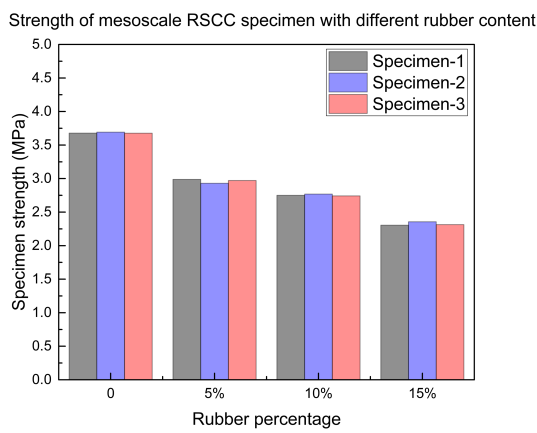
662

663   (b) Column chart of specimen strength with different rubber content

664   **Fig. 8.** Simulation result of RSCC with different rubber content under uniaxial tension

665
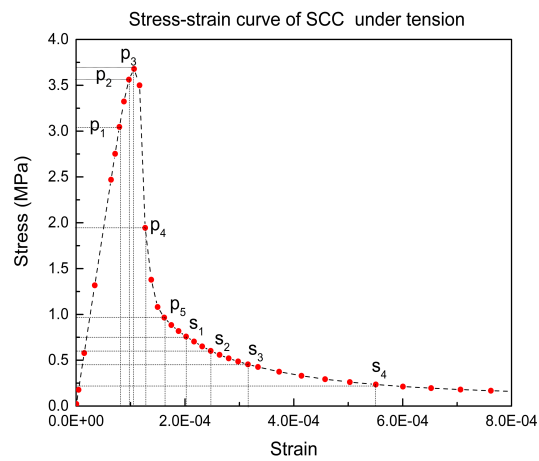
666
667   (a) Stress-strain curve of RSCC-0
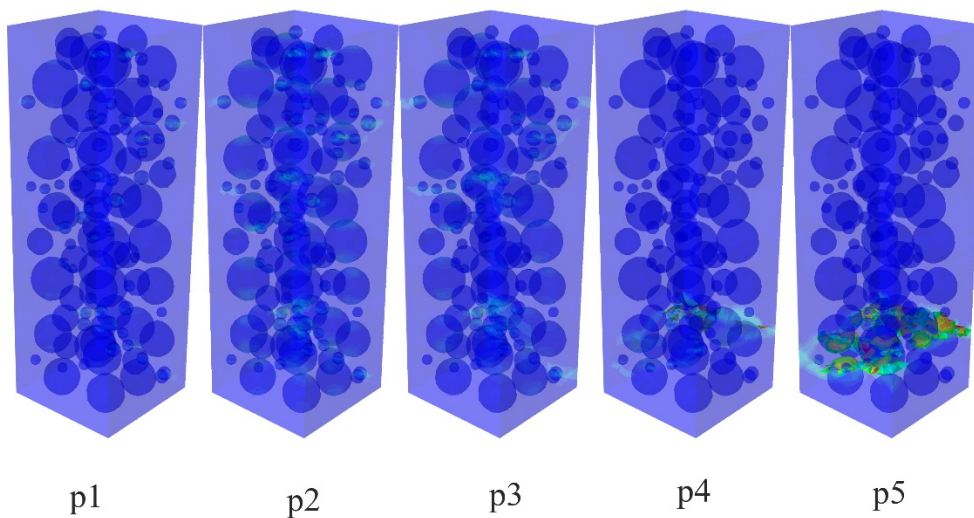
                p1   p2   p3   p4   p5

668
669   (b) Microcrack development status of mesoscale RSCC-0 specimen at time p0, p1, p2, p3, p4, p5
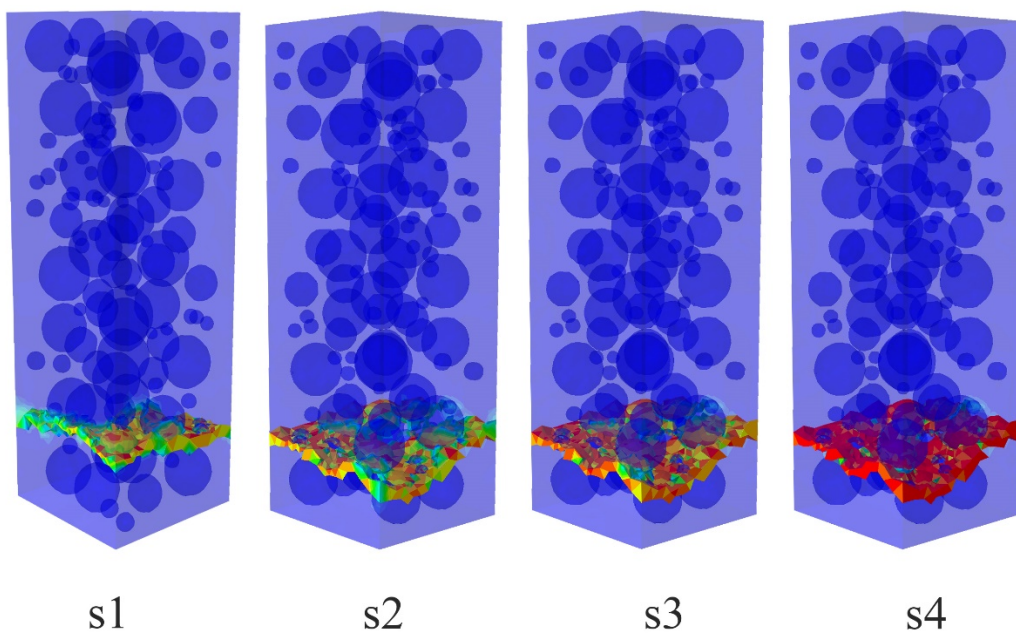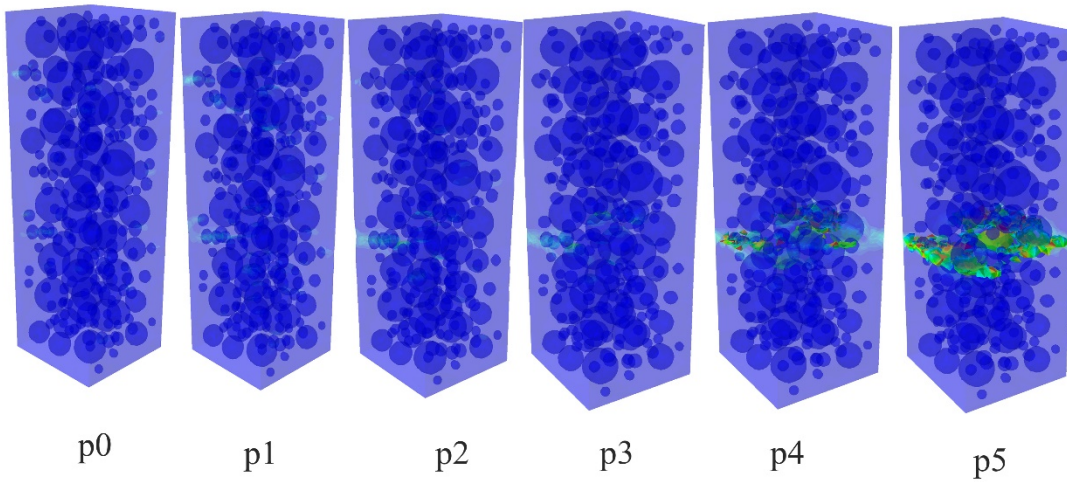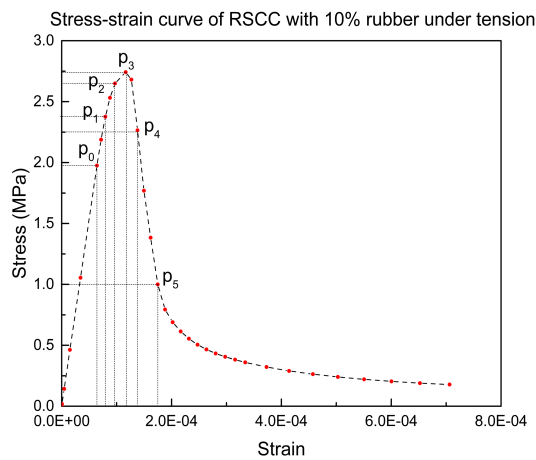

670   s1   s2   s3   s4

671   (c) Macrocrack development status of mesoscale RSCC-0 specimen at time s1, s2, s3, s4

672   **Fig. 9.** Simulation result of RSCC-0 specimen under uniaxial tension
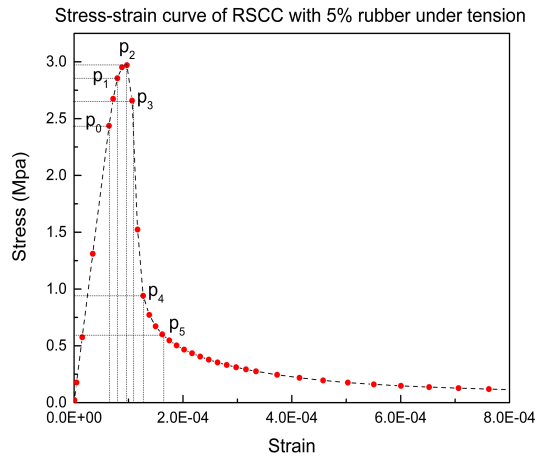
673

674   (a) Stress-strain curve of RSCC-5
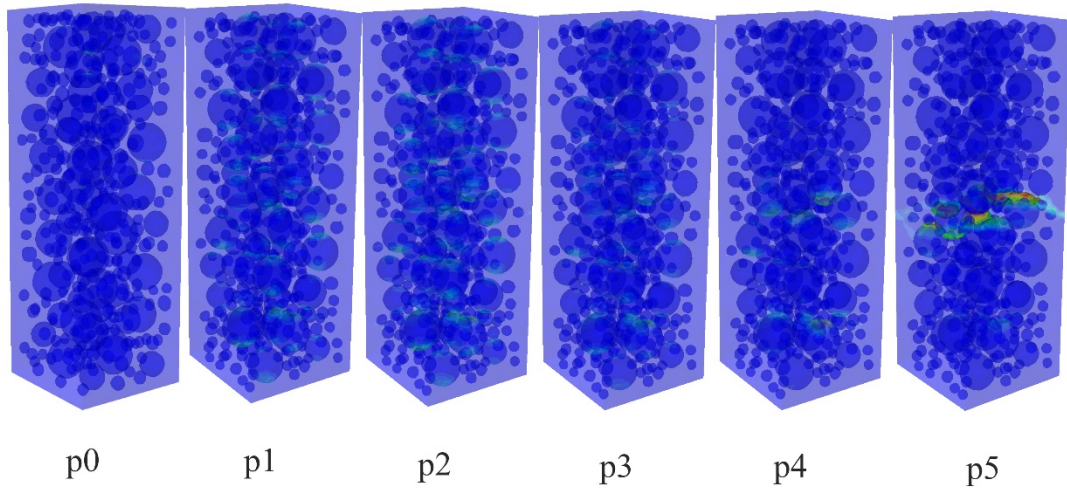

675

676   (b) Microcrack development status of mesoscale RSCC-5 specimen at time p0, p1, p2, p3, p4, p5

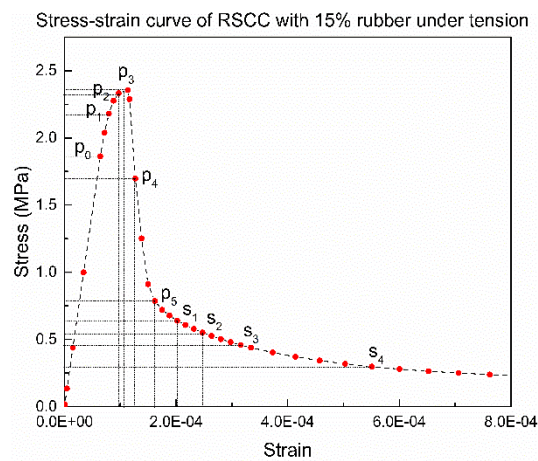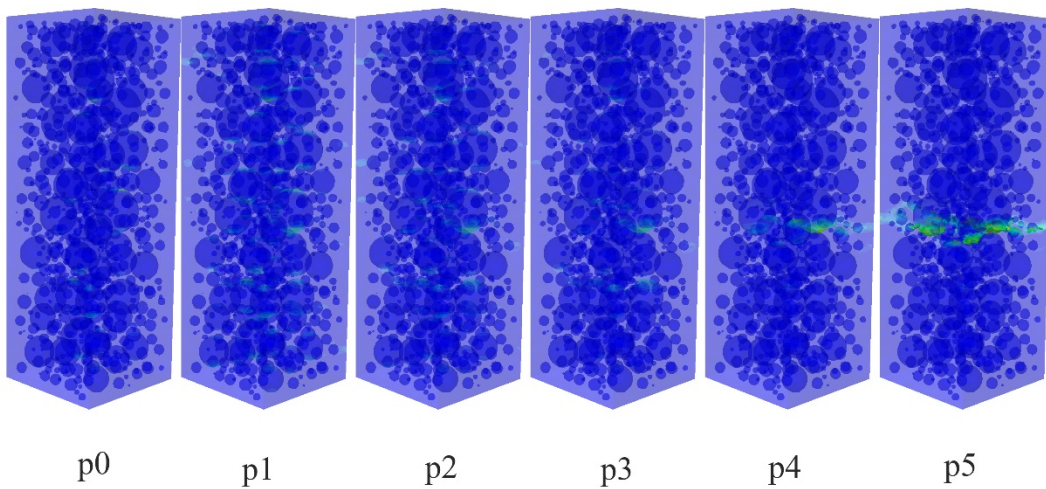677   **Fig. 10.** Simulation result of RSCC-5 specimen under uniaxial tension

678

679   (a) Stress-strain curve of RSCC-5

680

p0   p1   p2   p3   p4   p5

681
682

683   (b) Microcrack development status of mesoscale RSCC-10 specimen at time p0, p1, p2, p3, p4,

684   p5

685   **Fig. 11.** Simulation result of RSCC-10 specimen under uniaxial tension

686

687   (a) Stress-strain curve of RSCC-5

688

p0   p1   p2   p3   p4   p5
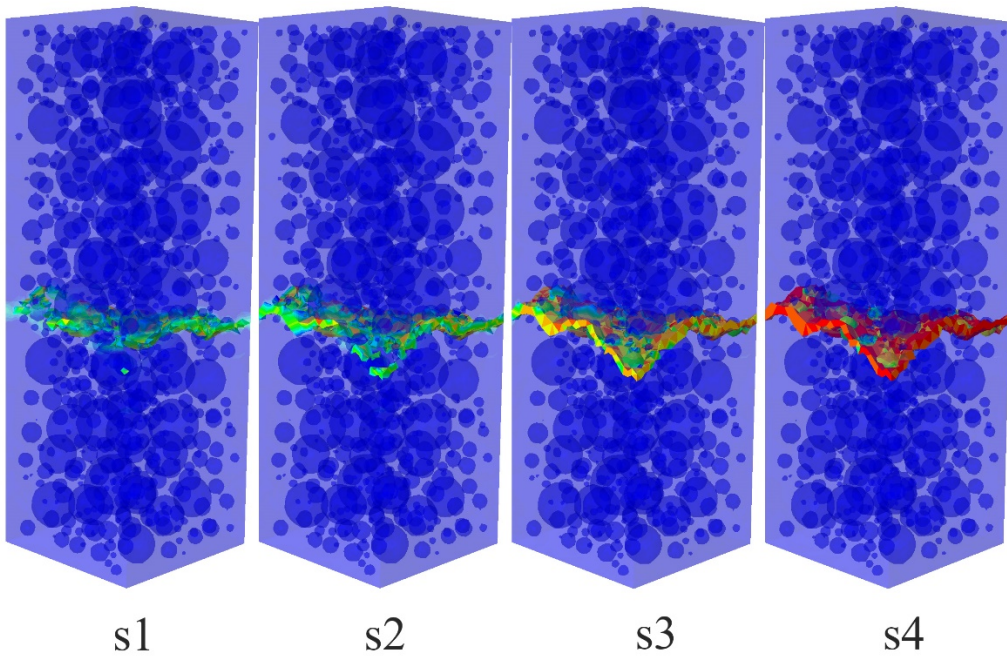
689

690   (b) Microcrack development status of mesoscale RSCC-15 specimen at time p0, p1, p2, p3, p4,

691

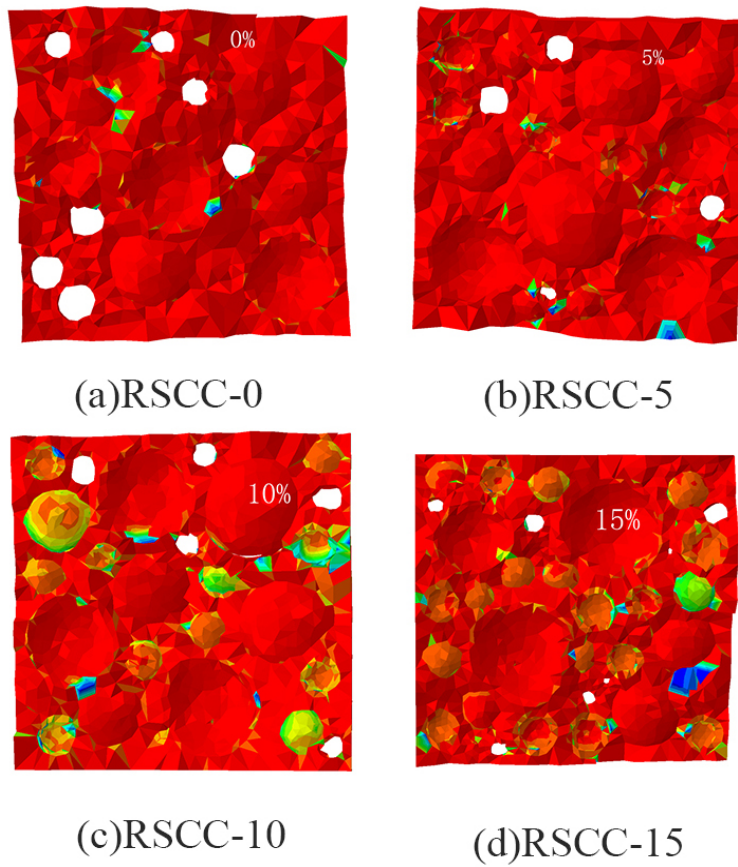s1   s2   s3   s4

692

693   (c) Macrocrack development status of mesoscale RSCC-15 specimen at time s1, s2, s3, s4

694   **Fig. 12.** Simulation result of RSCC-15 specimen under uniaxial tension

(a)RSCC-0   (b)RSCC-5

(c)RSCC-10   (d)RSCC-15

695

696   **Fig. 13.** Final crack morphology of RSCC specimens with different rubber content